

Scaling behavior of dissipative systems with imaginary gap closing

Jinghui Pi,^{1, 2,*} Xingli Li,^{2, 1} and Yangqian Yan^{2, 3, 1, †}

¹*The Chinese University of Hong Kong Shenzhen Research Institute, 518057 Shenzhen, China*

²*Department of Physics, The Chinese University of Hong Kong, Shatin, New Territories, Hong Kong, China*

³*State Key Laboratory of Quantum Information Technologies and Materials,
The Chinese University of Hong Kong, Hong Kong SAR, China*

Point-gap topology, characterized by spectral winding numbers, is crucial to non-Hermitian topological phases and dramatically alters real-time dynamics. In this paper, we study the evolution of quantum particles in dissipative systems with imaginary gap closing, using the saddle-point approximation method. For trivial point-gap systems, imaginary gap-closing points can also be saddle points. This leads to a single power-law decay of the local Green's function, with the asymptotic scaling behavior determined by the order of these saddle points. In contrast, for nontrivial point-gap systems, imaginary gap-closing points do not coincide with saddle points in general. This results in a dynamical behavior characterized by two different scaling laws for distinct time regimes. In the short-time regime, the local Green's function is governed by the dominant saddle points and exhibits an asymptotic exponential decay. In the long-time regime, however, the dynamics is controlled by imaginary gap-closing points, leading to a power-law decay envelope. Our findings advance the understanding of quantum dynamics in dissipative systems and provide predictions testable in future experiments.

I. INTRODUCTION

Non-Hermitian physics has achieved substantial progress over the past two decades [1–7]. For instance, non-Hermitian Hamiltonians describe optical systems with gain and loss [8–13], dissipative wave dynamics in classical networks [14–24], and quasiparticle dynamics in condensed matter systems [25–31]. A prominent feature of such lattice systems is the non-Hermitian skin effect (NHSE) [32–37], which refers to the localization of an extensive number of eigenstates at the edges under the open boundary condition (OBC). This anomalous boundary localization phenomenon is closely related to the point-gap topology of non-Hermitian Bloch Hamiltonians [38–41], causing a high sensitivity of the spectrum to boundary conditions and reshaping the conventional bulk-boundary correspondence [16, 42–51]. Another unique feature of dissipative quantum systems is the closing of the Liouvillian gap (or imaginary gap) [52–55], which results in algebraic damping behavior and a divergence of the relaxation time [56–64].

Notably, boundary effects also induce distinctive non-Hermitian dynamical phenomena, including unidirectional amplification [65–67], enhanced quantum sensing [68–71], and novel dynamics of entanglement [72–76] and wave packet propagation [77–81]. During time evolution, the influence of boundary terms diminishes with increasing system size, rendering non-Hermitian dynamics independent of boundary conditions in the thermodynamic limit [82]. This behavior is intuitive for trivial point-gap systems, as their energy spectra are also independent of boundary conditions in this limit.

In contrast, for nontrivial point-gap systems, energy spectra under OBC differ significantly from those under periodic boundary conditions (PBC) [38–41]. For finite-sized systems, it is unclear how to detect this spectral discrepancy and incorporate boundary effects through a real-time dynamical process. Moreover, for systems with imaginary gap closing, the distinction in bulk dynamics between trivial and nontrivial point-gap phases also remains largely unexplored.

In this work, we investigate the long-time dynamics of quantum particles initially released at bulk sites of dissipative systems with imaginary gap closing. To facilitate the analysis of these systems, we introduce the non-Hermitian multi-band Green's function and the concept of point-gap topology. For systems with a trivial point gap, the imaginary gap-closing points can also be saddle points of the non-Hermitian Bloch Hamiltonian. In such cases, the local Green's function exhibits a power-law decay, scaling asymptotically as $t^{-1/n}$, where n is the order of the dominant saddle points. In contrast, for systems with a nontrivial point gap, the imaginary gap-closing points do not coincide with saddle points. As a result, the local Green's function demonstrates two distinct dynamical regimes. In the short-time regime, the evolution is governed by the dominant saddle points and shows an asymptotic exponential decay. Beyond this transient period, the influence of the boundary becomes significant. The subsequent dynamics are then controlled by the imaginary gap-closing points, and the local Green's function exhibits a power-law evolution. This long-time scaling is determined by the saddle point of the world-line Green's function, which is related to the group velocities at the corresponding imaginary gap-closing points. The aforementioned asymptotic scaling behavior in imaginary gap-closing systems is derived theoretically using the saddle-point approximation and is confirmed numerically. Our findings enhance the

* pijh14@gmail.com

† yqyan@cuhk.edu.hk

understanding of quantum dynamics in dissipative systems and provide a theoretical foundation for future experimental observation of saddle-point dynamics in non-Hermitian systems.

The remainder of this paper is organized as follows. In Sec. II, we present the general form of the non-Hermitian Green's function in the time domain and a brief introduction to point-gap topology. The long-time dynamics of imaginary gap-closing systems are then analyzed for two cases, based on the saddle point approximation of the Green's function. In Sec. III, we study the scaling behavior in systems with trivial point-gap topology using a concrete dissipative two-band model. Sec. IV extends this analysis to systems with a nontrivial point-gap topology via an associated two-band model. Finally, a summary of the main conclusions and an outlook for future work are provided in Sec. V.

II. MULTI-BAND REAL-TIME GREEN FUNCTIONS AND POINT-GAP TOPOLOGY

For a generic one-dimensional (1D) multiband non-Hermitian tight-binding system, the real-space Hamiltonian reads:

$$H = \sum_{x,y} \sum_{a,b}^q t_{y-x}^{ab} |x, a\rangle \langle y, b|, \quad (1)$$

where x and y denote the spatial locations of the unit cells, and $a, b = 1, 2, \dots, q$ represent the internal orbitals within each unit cell. The hopping amplitude t_{y-x}^{ab} has a finite range and vanishes for $|y - x| > N$. The system's evolution can be captured by the single-particle Green's function in the time domain, which is defined as

$$G_{ab}(x, y; t) = \langle x, a | e^{-iHt} | y, b \rangle. \quad (2)$$

By imposing periodic boundary conditions and performing a Fourier transformation, the Green's function (2) in the thermodynamic limit can be recast as an integral over the Brillouin zone (BZ):

$$\begin{aligned} G_{ab}(x, y; t) &= \int_0^{2\pi} \frac{dk}{2\pi} e^{ik(x-y)} \langle a | e^{-ih(k)t} | b \rangle \\ &= \oint_{|\beta|=1} \frac{d\beta}{2\pi i \beta} \beta^{x-y} \langle a | e^{-ih(\beta)t} | b \rangle, \end{aligned} \quad (3)$$

where $\beta = e^{ik}$ is the Bloch phase factor and $h(\beta)_{ab} = \sum_{l=-N}^N t_l^{ab} \beta^l$ is the non-Hermitian Bloch Hamiltonian. To calculate the integral (3), we can diagonalize $h(\beta)$ using its left and right eigenstates. As a result, the matrix element of the time evolution operator $e^{-ih(\beta)t}$ becomes

$$\langle a | e^{-ih(\beta)t} | b \rangle = \sum_{n=1}^q e^{-iE_n(\beta)t} R_{n,a}(\beta) L_{n,b}(\beta), \quad (4)$$

where $R_{n,a}(\beta) = \langle a | R_n(\beta) \rangle$, $L_{n,b}(\beta) = \langle L_n(\beta) | b \rangle$, and $E_n(\beta)$ is the n -th band eigenvalue of $h(\beta)$. Here, $\langle L_n(\beta) |$

and $|R_n(\beta)\rangle$ denote the corresponding left and right eigenstates. By defining $g_n^{ab}(\beta) = R_{n,a}(\beta) L_{n,b}(\beta)$, we obtain a compact representation of the Green's function:

$$G_{ab}(x, y; t) = \sum_n \oint_{|\beta|=1} \frac{d\beta}{2\pi i \beta} \beta^{x-y} g_n^{ab}(\beta) e^{-iE_n(\beta)t}. \quad (5)$$

For a system with onsite dissipation, the energy spectrum is bounded by the condition $\text{Im}[E_n(\beta)] \leq 0$. Especially, if points β_0 exist in the BZ such that $\text{Im}[E_n(\beta_0)] = 0$ for some band E_n , the imaginary (dissipative) gap of the system is closed. We focus on this case in the remainder of this paper.

An important concept in non-Hermitian topological phases is the point gap, which is characterized by a winding number of the spectrum in the complex energy plane. Specifically, for a reference point $E_b \in \mathbb{C}$, the following winding number can be defined over the BZ [38, 39, 46]:

$$W(E_b) = \oint_{|\beta|=1} \frac{d\beta}{2\pi i} \partial_\beta \ln \det[h(\beta) - E_b]. \quad (6)$$

If $W(E_b) = 0$ for all $E_b \in \mathbb{C}$, the point-gap of the system is trivial. In this case, the spectrum under PBC collapses onto the spectrum under OBC in the thermodynamic limit. In contrast, if $W(E_b) \neq 0$ for a given E_b , the system possesses a nontrivial point gap, implying that the PBC spectrum encloses a finite area in the complex energy plane. Consequently, the corresponding OBC spectrum is enclosed by the PBC spectrum, and the eigenstates feature the NHSE [39, 46]. To obtain the OBC spectra from the non-Hermitian Bloch Hamiltonian $h(\beta)$, one can use the concept of the generalized Brillouin zone (GBZ). For a given energy E , the characteristic equation $f(\beta, E) = \det[h(\beta) - E] = 0$ yields $2M = 2qN$ solutions. When these solutions are ordered by their magnitude, $|\beta_1(E)| \leq |\beta_2(E)| \leq \dots \leq |\beta_{2M}(E)|$, the GBZ is determined by the condition $|\beta_M(E)| = |\beta_{M+1}(E)|$ [32, 45, 46], which traces a closed curve in the complex β -plane.

III. SCALING BEHAVIOR OF IMAGINARY GAP-CLOSING SYSTEMS WITH A TRIVIAL POINT-GAP TOPOLOGY

In this section, we discuss imaginary gap-closing systems with a trivial point gap. For concreteness, we consider a one-dimensional lossy lattice ladder, as shown in Fig. 1(a). The tight-binding Hamiltonian reads:

$$\begin{aligned} H = & \sum_n \left(t_0 c_{n,A}^\dagger c_{n,B} + t_1 c_{n+1,A}^\dagger c_{n,B} + t_1 c_{n-1,A}^\dagger c_{n,B} \right) \\ & + \text{H.c.} - \sum_n i\gamma c_{n,B}^\dagger c_{n,B}, \end{aligned} \quad (7)$$

where t_0 and t_1 are the intracell and intercell hopping amplitudes, respectively, γ is the onsite dissipation on

sublattice B, and H.c. denotes the Hermitian conjugate. By applying a Fourier transformation and making the substitution $e^{ik} \rightarrow \beta$, we obtain the generalized non-Hermitian Bloch Hamiltonian:

$$h(\beta) = h_x(\beta) \sigma_x + \frac{i\gamma}{2} \sigma_z - \frac{i\gamma}{2} I, \quad (8)$$

where $h_x(\beta) = t_0 + t_1(\beta + \beta^{-1})$. Here, $\sigma_{x,y,z}$ are the Pauli matrices, with sublattice A (B) corresponding to the up (down) component of a pseudo-spin, while I denotes the identity matrix. The energy spectrum of Eq. (8) is

$$E_{\pm}(\beta) = -\frac{i\gamma}{2} \pm \sqrt{h_x^2(\beta) - \frac{\gamma^2}{4}}, \quad (9)$$

which consists of several open curves in the complex energy plane, as shown in Figs. 1(b) and 1(c). Hence, the point gap of the system is always trivial; that is, the winding number $W(E_b)$ defined in Eq. (6) is equal to zero for any arbitrary complex reference energy $E_b \in \mathbb{C}$. As a result, the energy spectra under both OBCs and PBCs collapse to the same curves in the thermodynamic limit, implying the absence of the NHSE. Due to the dissipative nature of the system, the imaginary part of the energy must be less than or equal to zero, that is, $\text{Im} E_{\pm}(\beta) \leq 0$. In particular, when $h_x(\beta) = 0$, the Bloch energy spectrum (9) touches the real axis (i.e., $\max[\text{Im} E_{\pm}(\beta)] = 0$), thus closing the imaginary gap [64]. Given that $|\cos k| \leq 1$, this condition is satisfied only when $|t_0| \leq |2t_1|$.

On the other hand, at the saddle points of the Bloch Hamiltonian (8), we have $\frac{dE_{\pm}(\beta)}{d\beta}|_{\beta=\beta_s} = 0$, which requires

$$h_x(\beta_s)(1 - \beta_s^{-2}) = 0. \quad (10)$$

Thus, in addition to the solutions $\beta_s = \pm 1$, any other saddle points should satisfy $h_x(\beta_s) = 0$. This implies that the system's imaginary gap-closing points are also its saddle points. However, the converse is not necessarily true. This distinction arises because imaginary gap-closing points are restricted to the unit circle $|\beta| = 1$, whereas saddle points can exist anywhere in the complex β plane. For instance, when $|t_0| > |2t_1|$, the equation $h_x(\beta_s) = 0$ yields two roots with $|\beta| \neq 1$. In this scenario, the system has saddle points but lacks imaginary gap-closing points. Furthermore, the configuration of saddle points exhibits two distinct behaviors depending on the system's parameters. For $|t_0| < |2t_1|$, equation $h_x(\beta_s) = 0$ has two distinct solutions, $\beta_s = e^{\pm ik_s}$, where $\cos k_s = -t_0/(2t_1)$. These solutions lie on the unit circle and correspond to two imaginary gap-closing points at an energy of $E_+(\beta) = 0$, as shown in Fig. 1(b). In contrast, at the critical parameters $|t_0| = |2t_1|$, the equation for saddle points (10) has a threefold degenerate solution $\beta_s = -1$. This point also corresponds to an imaginary gap closing at $E_+(\beta) = 0$, as shown in Fig. 1(c).

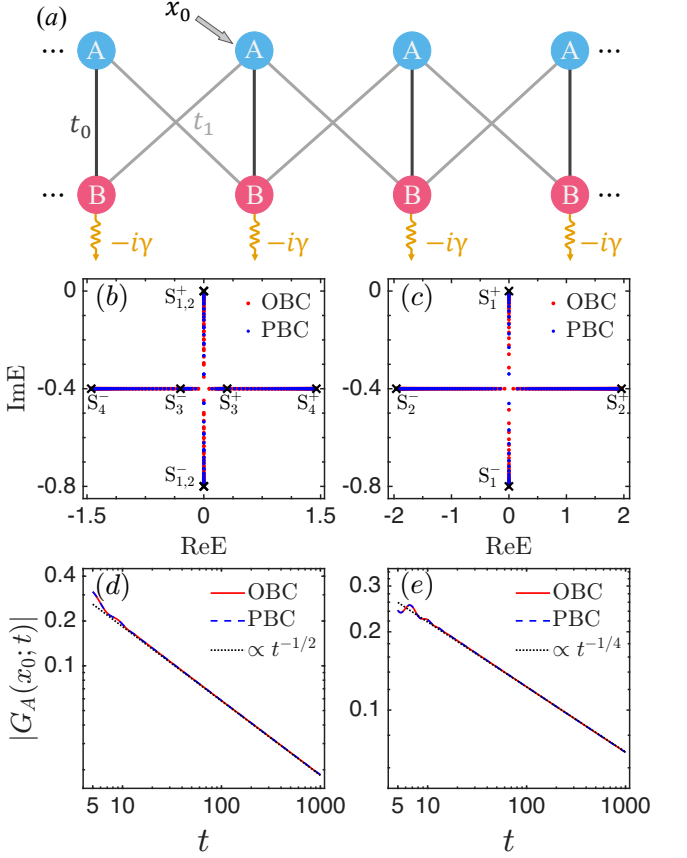


FIG. 1. (a) Schematic of a one-dimensional lossy ladder lattice with trivial point-gap topology, which corresponds to the Hamiltonian in Eq. (7). Each unit cell, labeled by the spatial coordinate x , comprises two sites, denoted A and B. The particle is initially localized on the A sublattice of the unit cell at x_0 . The energy spectra and corresponding numerical results for the local Green's function $G_A(x_0; t) = \langle x_0, A | e^{-iHt} | x_0, A \rangle$ are as follows: (b)-(c) OBC (red points) and PBC (blue points) energy spectra E_{\pm} , with saddle points S_i^{\pm} explicitly marked by cross symbols. The saddle points S_1^+ and S_2^+ in (b), as well as the threefold saddle point S_1^+ in (c), are also imaginary gap-closing points. (d)-(e) Numerical results for the scaling of $|G_A(x_0; t)|$ with bulk $x_0 = 75$ under OBC (red solid lines) and PBC (blue dashed lines); these agree well with the theoretical results (black dashed lines). In (b) and (d), the parameters are $t_0 = 0.5, t_1 = 0.5$, and $\gamma = 0.8$; in (c) and (e), $t_0 = 1.0, t_1 = 0.5$, and $\gamma = 0.8$. The number of unit cells is $L = 150$ for the numerical calculation.

We now examine the dynamic behavior of a wave packet along the 1D ladder governed by the Hamiltonian in Eq. (7). The initial state is a delta function localized at the non-decaying sublattice A of the bulk x_0 , such that $\psi_x^A(0) = \delta_{x,x_0}$ and $\psi_x^B(0) = 0$. In this dissipative system, the amplitude at the initial site is defined as $\langle x_0, A | e^{-iHt} | x_0, A \rangle$. This corresponds to the time-domain local Green's function $G_{AA}(x_0, x_0; t)$ (abbreviated as $G_A(x_0; t)$ for simplicity), which can be probed in experimental systems [83]. As a result, in the thermodynamic limit (i.e., for a large system size), the

local Green's function $G_A(x_0; t)$ under PBC takes the form of

$$G_A(x_0; t) = \sum_{n=\pm} \oint_{|\beta|=1} \frac{d\beta}{2\pi i \beta} g_n^{AA}(\beta) e^{-iE_n(\beta)t}, \quad (11)$$

where $g_n^{AA}(\beta) = \langle A|R_n(\beta)\rangle\langle L_n(\beta)|A\rangle$, with $|R_n(\beta)\rangle$ and $\langle L_n(\beta)|$ denoting the right and left eigenstates of the Bloch Hamiltonian (8), respectively. To evaluate the long-time behavior of the contour integrals in Eq. (11), the steepest descent method is a commonly employed approach (see Appendix B for further details) [84]. The fundamental principle involves the deformation of the original integral path $|\beta|=1$ into a new path \mathcal{C}' in the complex β plane. This deformation adheres to two key conditions: (i) the contour \mathcal{C}' passes through a saddle point β_s , where $\text{Im } E_n(\beta_s) \geq \text{Im } E_n(\beta)$ for all $\beta \in \mathcal{C}'$; (ii) the real part of $E_n(\beta)$ remains constant along the path \mathcal{C}' , namely $\text{Re } E_n(\beta) = \text{Re } E_n(\beta_s)$ for all $\beta \in \mathcal{C}'$. Hence, this new path must represent the steepest descent direction of $\text{Im } E_n(\beta)$ from the saddle point β_s (see more details in Appendix A). Then, for large t , it follows that the contour integral is asymptotically dominated by this saddle point, yielding:

$$\oint_{|\beta|=1} \frac{g_n^{AA}(\beta)}{2\pi i \beta} e^{-iE_n(\beta)t} d\beta \xrightarrow{t \rightarrow \infty} \alpha t^{-\frac{1}{2}} e^{-iE_n(\beta_s)t}, \quad (12)$$

where $\alpha = \frac{g_n^{AA}(\beta_s)}{\beta_s \sqrt{2\pi i^3 E_n''(\beta_s)}}$, provided that $g_n^{AA}(\beta_s) \neq 0$ and $E_n''(\beta_s) \equiv \frac{d^2 E_n(\beta)}{d\beta^2}|_{\beta=\beta_s} \neq 0$.

When the imaginary gap-closing condition is satisfied, the contribution of the $E_+(\beta)$ band to the contour integral in Eq. (11) is dominated by the corresponding saddle point where $E_+(\beta) = 0$. If $|t_0| < |2t_1|$, we can select a deformed contour \mathcal{C}' that passes through this saddle point and apply the steepest descent method. This yields a power-law decay scaling of $t^{-1/2}$ for the contour integral of the $E_+(\beta)$ band. Since $\text{Im } E_-(\beta) \leq -\gamma/2$, the contribution of the $E_-(\beta)$ band contour integral in Eq. (11) becomes exponentially small for large t and can, therefore, be neglected. Consequently, in the long time limit, the local Green's function $G_A(x_0; t)$ exhibits the following asymptotic power-law scaling behavior:

$$\lim_{t \rightarrow \infty} G_A(x_0; t) \propto t^{-1/2}, \quad (13)$$

provided that $|t_0| < |2t_1|$. We numerically calculate $G_A(x_0; t)$ under both PBC and OBC. In Fig. 1(d), we show that the results for both conditions collapse onto nearly identical evolution curves and agree well with the scaling of the theoretically predicted $t^{-1/2}$ power-law at large t .

However, the aforementioned steepest descent method fails when $|t_0| = |2t_1|$. At these critical parameters, the imaginary gap-closing energy corresponds to a fourth-order saddle point at $\beta_s = -1$, leading to the vanishing of

the second-order derivative, $\frac{d^2 E_+(\beta)}{d\beta^2}|_{\beta=-1}$. In this case, the long-time asymptotic behavior of the contour integral $\oint_{|\beta|=1} \frac{g_+^{AA}(\beta)}{2\pi i \beta} e^{-iE_+(\beta)t} d\beta$ is still dominated by this fourth-order saddle point. To evaluate this integral, we expand $E_+(\beta)$ near $\beta_s = -1$. In the neighborhood of this point, $E_+(\beta) \approx \frac{E_+^{(4)}(-1)}{4!} (\beta - 1)^4$, where $E_+^{(4)}(-1) = \frac{d^4 E_+(\beta)}{d\beta^4}|_{\beta=-1}$. Therefore, a modified steepest descent method is required. By deforming the contour $|\beta|=1$ into the steepest descent path \mathcal{C}' around the fourth-order saddle point $\beta_s = -1$, in the large t limit, the leading order contribution of the integral is given by [84]

$$\lim_{t \rightarrow \infty} \oint_{|\beta|=1} \frac{g_+^{AA}(\beta)}{2\pi i \beta} e^{-iE_+(\beta)t} d\beta \sim \alpha' t^{-\frac{1}{4}}, \quad (14)$$

where $\alpha' = -\frac{g_+^{AA}(-1)\Gamma(1/4)}{8\pi i \left[-E_+^{(4)}(-1)/24\right]^{1/4}}$. As a result, the asymptotic scaling of the local Green's function $G_A(x_0; t)$ at these critical values $|t_0| = |2t_1|$ is

$$\lim_{t \rightarrow \infty} G_A(x_0; t) \propto t^{-1/4}. \quad (15)$$

This theoretical prediction agrees closely with the numerical calculations in the long time limit, for both PBC and OBC, as shown in Fig. 1(e).

The aforementioned results can, in fact, be extended to a more general dissipative model. Specifically, if the imaginary gap-closing point is also an n -th order saddle point β_s of the energy band $E_m(\beta)$, the local Green's function $G_A(x_0; t)$ can be evaluated using a higher-order saddle point approximation. An n -th order saddle point is defined by the conditions $E_m^{(p)}(\beta_s) = 0$ for $p = 1, 2, \dots, n-1$, and $E_m^{(n)}(\beta_s) \neq 0$, where $E_m^{(p)}(\beta_s) = (d^p E_m/d\beta^p)|_{\beta=\beta_s}$. Applying the approximation yields the following asymptotic expression [84]:

$$G_A(x_0; t) \sim \frac{g_m^{AA}(\beta_s) \Gamma(1/n)}{n \left[-E_m^{(n)}(\beta_s)/(n!) \right]^{1/n}} t^{-1/n}, \quad (16)$$

implying that the long time evolution of $G_A(x_0; t)$ exhibits a characteristic scaling behavior of $t^{-1/n}$.

The above discussion does not always hold for imaginary gap-closing systems with a trivial point-gap topology. In fact, at these imaginary gap-closing points β_0 , we have $\text{Im } \partial_\beta E(\beta)|_{\beta=\beta_0} = 0$. Hence, if $\text{Re } \partial_\beta E(\beta)|_{\beta=\beta_0} = 0$, these points are also saddle points and correspond to the endpoints of the energy spectrum $E(\beta)$. However, it is also possible that $\text{Re } \partial_\beta E(\beta)|_{\beta=\beta_0} \neq 0$, which means that β_0 is not a saddle point of $E(\beta)$. In this case, the energy spectrum $E(\beta)$ is tangent to the $\text{Re } E$ axis at β_0 in the complex plane.

IV. SCALING BEHAVIOR OF IMAGINARY GAP-CLOSING SYSTEMS WITH A NONTRIVIAL POINT-GAP TOPOLOGY

We now consider imaginary gap-closing systems with a nontrivial point-gap topology. As a concrete example, the model discussed here is also a two-band model (see Fig. 2). The tight-binding Hamiltonian reads:

$$H_1 = H + \sum_n \left(t_p e^{i\phi} c_{n+1,A}^\dagger c_{n,A} + t_p e^{-i\phi} c_{n,A}^\dagger c_{n+1,A} + t_p e^{-i\phi} c_{n+1,B}^\dagger c_{n,B} + t_p e^{i\phi} c_{n,B}^\dagger c_{n+1,B} \right), \quad (17)$$

where the hopping term t_p between sites on the same sublattice carries a Peierls phase, generating fluxes ϕ through the triangular plaquettes. After applying a Fourier transformation and substitution $\beta \rightarrow e^{ik}$, we obtain the generalized non-Hermitian Bloch Hamiltonian

$$h_1(\beta) = h_x(\beta) \sigma_x + h_z(\beta) \sigma_z + h_0(\beta) I, \quad (18)$$

with

$$\begin{aligned} h_x(\beta) &= t_0 + t_1(\beta + \beta^{-1}), \\ h_z(\beta) &= it_p \sin \phi(\beta - \beta^{-1}) + i\gamma/2, \\ h_0(\beta) &= t_p(\beta + \beta^{-1}) \cos \phi - i\gamma/2. \end{aligned}$$

The spectrum corresponding to this Hamiltonian is

$$E_{1,\pm}(\beta) = h_0(\beta) \pm \sqrt{h_x^2(\beta) + h_z^2(\beta)}. \quad (19)$$

Due to nonzero fluxes ϕ , this system breaks the time-reversal symmetry. Intuitively, the fluxes ϕ within the triangular plaquettes induce rotational motions, causing the A and B chains to favor propagation in opposite directions. The loss term then generates a net chiral motion along the A chain by suppressing the backflow on the B chain. Hence, onsite dissipation γ induces NHSE under OBC [85]. As a result, the PBC spectrum exhibits a nontrivial point-gap topology and differs dramatically from its OBC counterpart. This is in sharp contrast to the trivial point-gap model in Sec. III. To elucidate this distinction and facilitate a clear discussion, we set $\phi = \pi/2$ for the remainder of this section. As shown in Figs. 3(a) and 3(b), two typical spectral configurations emerge: the PBC spectra form either one or two closed loops, while the OBC spectra consist of two open arcs enclosed by these PBC loops.

The imaginary gap-closing condition of this system remains $h_x(\beta) = 0$ [64], that is, $|t_0| \leq |2t_1|$. However, these imaginary gap-closing points are generally not saddle points of the corresponding nontrivial point-gap system. For $\phi = \pi/2$, the saddle points defined by $\frac{dE_{1,\pm}(\beta)}{d\beta}|_{\beta=\beta_s} = 0$ satisfy the following equation:

$$h_x(\beta_s) h'_x(\beta_s) + h_z(\beta_s) h'_z(\beta_s) = 0. \quad (20)$$

For nonzero t_0 , the solutions of this equation do not lie in the unit circle $|\beta| = 1$, implying that the corresponding

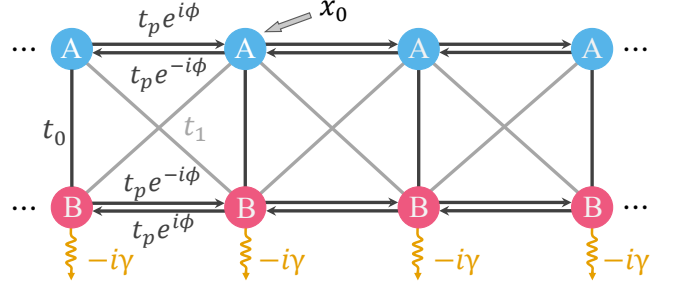


FIG. 2. Schematic of a one-dimensional lossy ladder lattice with nontrivial point-gap topology, which corresponds to the Hamiltonian in Eq. (17). A nonzero Peierls phase ϕ is introduced via the hopping term t_p , which breaks the time-reversal symmetry of the system.

energies are not part of the PBC spectrum. In contrast, the endpoints of the OBC spectra are attained for values of β on the GBZ that correspond to the saddle points of $E_{1,\pm}(\beta)$, as shown in Figs. 3(a) and 3(b). For a general model, not all saddle points are located on the GBZ [86, 87]. In fact, the corresponding characteristic equation $\det[h(\beta) - E] = 0$ gives an exact relation between E and β . The saddle points are independent of the boundary conditions and are uniquely determined by the equation $\partial_\beta E(\beta) = 0$, indicating that they correspond to double roots of the characteristic equation. Hence, these saddle points typically reside on the auxiliary generalized Brillouin zone (aGBZ) [88–90].

The dynamics of such a nontrivial point-gap model also exhibit distinct features compared to the trivial point-gap model discussed in Sec. III. Here, we still consider the time evolution of the system under the initial conditions $\psi_x^A(0) = \delta_{x,x_0}$ and $\psi_x^B(0) = 0$. The local Green's function $G_A(x_0; t)$ exhibits different scaling behavior on two distinct time scales. In the short-time regime, the wave packet propagates within a finite range of the lattice and does not traverse the entire system. Thus, as evidenced in Figs. 3(c) and 3(d), the dynamics of the local Green's function $G_A(x_0; t)$ are identical for both PBC and OBC. This equivalence allows for the treatment of the system as an infinitely extended lattice, where the discrete momentum k can be approximated by a continuous variable. It follows that $G_A(x_0; t)$ admits an integral representation:

$$G_A(x_0; t) = \sum_{n=\pm} \oint_{|\beta|=1} \frac{d\beta}{2\pi i \beta} g_{1,n}^{AA}(\beta) e^{-iE_{1,n}(\beta)t}, \quad (21)$$

where $g_{1,n}^{AA}(\beta) = \langle A|R_{1,n}(\beta)\rangle \langle L_{1,n}(\beta)|A\rangle$, with $|R_{1,n}(\beta)\rangle$ and $\langle L_{1,n}(\beta)|$ denoting the right and left eigenstates of the Bloch Hamiltonian (18), respectively. The asymptotic form of Eq. (21) can also be evaluated using the steepest descent method. Applying the complex Morse lemma [91, 92], the integral can be simplified by retaining the leading-order contributions

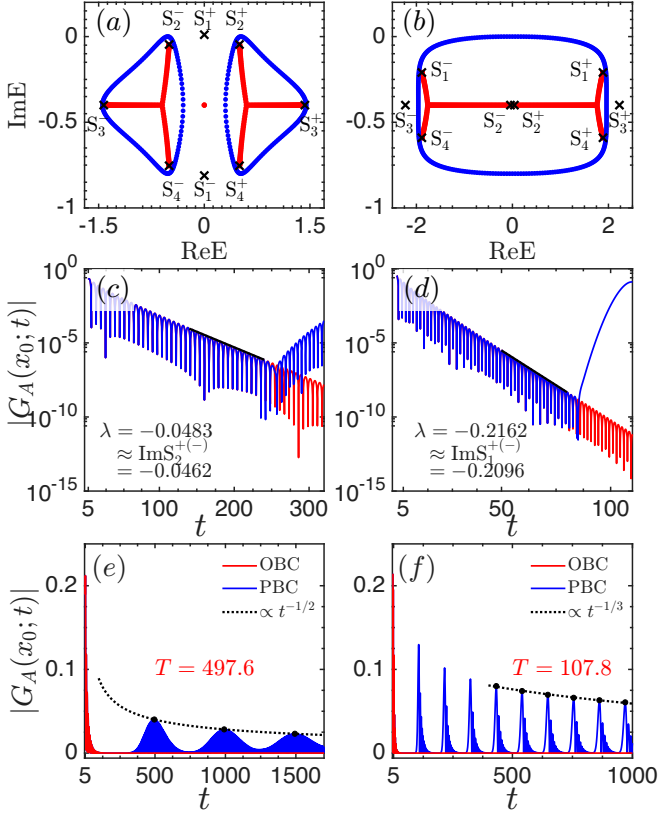


FIG. 3. Energy spectra and corresponding numerical results of $G_A(x_0; t)$ in an imaginary gap-closing system with nontrivial point-gap topology. (a)-(b) OBC (red points) and PBC (blue points) energy spectra E_{\pm} . Saddle points S_i^{\pm} are explicitly marked by cross symbols. With the exception of $\text{Im}S_1^+ = 0.01 > 0$ in (a), the imaginary parts of all other saddle points are negative. (c)-(d) Numerical results for short-time evolution of $|G_A(x_0; t)|$. The fitted values λ are in agreement with the theoretical saddle-point predictions. (e)-(f) Numerical results for long-time evolution of $|G_A(x_0; t)|$ exhibit a power law envelope, fitted by black dashed line. The local peaks within this envelope recur with a period T . In (a), (c), and (e), the parameters are $t_0 = 0.5$, $t_1 = 0.5$, $t_p = 0.3$, and $\gamma = 0.8$; in (b), (d), and (f), the parameters are $t_0 = 1.0$, $t_1 = 0.5$, $t_p = 0.7$, and $\gamma = 0.8$. For all panels, the Peierls phase is $\phi = \pi/2$ and the number of unit cells is $L = 150$.

from the neighborhood of the saddle point β_s , yielding:

$$G_A(x_0; t) \approx \sum_{n=\pm} \frac{g_{1,n}^{AA}(\beta_s)}{2\pi i \beta_s} e^{-iE_{1,n}(\beta_s)t} \sim e^{\text{Im}(S)t}, \quad (22)$$

where S is the dominant saddle point energy. Since the imaginary gap-closing point is not a saddle point, the selection of the appropriate saddle point through which the deformed contour \mathcal{C}' passes is subtle. One might naively identify the dominant saddle point as the one whose energy has the largest imaginary part. However, this conjecture is not always valid. For instance, as shown in Figs. 3(a) and 3(c), the saddle point energy S_1^+ has the largest imaginary part ($\text{Im}S_1^+ = 0.0111 > 0$) but

is clearly not the dominant saddle point. Instead, the short-time dynamics is governed by S_2^+ and S_2^- , which share an imaginary part of $\text{Im}S_2^+ = \text{Im}S_2^- = -0.0462$. This value is in reasonable agreement with the numerical decay rate, $\lambda = -0.0483$, extracted from the exponential envelope.

In fact, when multiple saddle points are present, the deformed integration contour \mathcal{C}' for each energy band $E_n(\beta)$ can be expressed as a linear combination of Lefschetz thimbles [93–98], such that $\mathcal{C}' = \sum_{\sigma} n_{\sigma} D_{\sigma}$. Here, each Lefschetz thimble D_{σ} is the steepest descent path of $\text{Im}E_n(\beta)$ originating from a corresponding saddle point $\beta_{s,\sigma}$. According to Morse theory, the coefficients n_{σ} are determined by the intersections between the deformed contour \mathcal{C}' (which is homologous to the original contour $|\beta| = 1$) and the steepest ascent path A_{σ} originating from the same saddle point. In particular, if A_{σ} intersects the integration domain $|\beta| = 1$ an even number of times, the intersections must occur from opposite directions, resulting in a zero net contribution, and therefore $n_{\sigma} = 0$. Consequently, the dominant saddle point can be identified as the one with a nonzero coefficient n_{σ} , whose associated energy possesses the largest imaginary part.

In the long-time regime, the wave packet delocalizes throughout the whole system. The local Green's function $G_A(x_0; t)$ exhibits distinct dynamical behaviors for different boundary conditions, and the system can no longer be treated as an infinitely long lattice. The saddle-point description thus becomes invalid, and the dynamics are instead dominated by imaginary gap-closing points, leading to algebraic decay behavior. Specifically, for $|t_0| < 2|t_1|$ and $t_0 \neq 0$, the numerical results show that $G_A(x_0; t)$ follows a $t^{-1/2}$ power-law envelope [see Fig. 3(e)]. In contrast, for $|t_0| = 2|t_1|$, the envelope of $G_A(x_0; t)$ changes to a decay scaling of $t^{-1/3}$, as shown in Fig. 3(f). Furthermore, for both types of scaling laws, the numerical results indicate that the peaks of $G_A(x_0; t)$ recur with a period T . These peaks are defined as the local maxima that conform to the envelope scaling. This periodicity is closely related to the imaginary gap-closing points, as will be discussed below.

For a general dissipative complex Bloch energy band $E_n(k)$, the imaginary part determines the attenuation of the wavefunction amplitude, while the real part is conventionally interpreted as a generalized energy. Accordingly, we define the group velocity $v_{n,g}(k)$, as the derivative of the real part of the energy:

$$v_{n,g}(k) = \frac{d}{dk} \text{Re}E_n(k), \quad k \in (0, 2\pi]. \quad (23)$$

This group velocity can be regarded as the characteristic speed of information propagation, and the absolute value of its maximum can be interpreted as the Lieb-Robinson bound for this non-Hermitian system [99, 100]. Therefore, the aforementioned steepest descent method is valid when the evolution time satisfies $t < L/(|v_{n,+}| + |v_{n,-}|)$, where $v_{n,+} = \max[v_{n,g}]$ and $v_{n,-}$

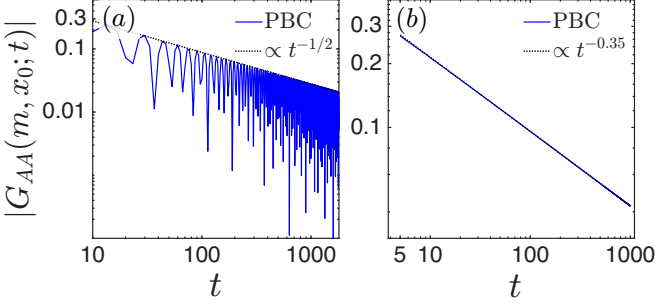


FIG. 4. Numerical results for the amplitude of world-line Green's function $G_{AA}(m, x_0; t)$ under PBC, where $m = x_0 + v_{n,g}(k_0)t$. Here, $v_{n,g}(k_0)$ is the group velocity at the imaginary gap-closing point for the E_n band. The parameter values are: $t_0 = 0.5$, $t_1 = 0.5$, $t_p = 0.3$, $\gamma = 0.8$, and $v_{+,g}(k_0) = v_{-,g}(k_0) = -0.3$ in (a); $t_0 = 1.0$, $t_1 = 0.5$, $t_p = 0.7$, $\gamma = 0.8$, and $v_{+,g}(k_0) = v_{-,g}(k_0) = -1.4$ in (b). For both panels, the initial conditions are $\psi_x^A(0) = \delta_{x,x_0}$ and $\psi_x^B(0) = 0$, with the number of unit cells is $L=150$.

$= \min[v_{n,g}]$ denote the maximum rightward and leftward propagation velocities, respectively. When the imaginary gap-closing condition is satisfied, eigenmodes with energy near these closing points decay the slowest and consequently govern the long-time dynamics. Therefore, we consider the group velocity at these imaginary gap-closing points, defined by k_0 where $\text{Im}E_n(k_0) = 0$, yielding $v_{n,g}(k_0)$. The time required for a particle, initially localized at a non-decaying position x_0 , to traverse a circle and return to x_0 via this imaginary gap-closing mode is $T = L/|v_{n,g}(k_0)|$. For the parameters selected in Figs. 4(e) and 4(f), the theoretical predictions show that $T = 500$ and $T = 107.1$, which are in reasonable agreement with the numerical results, $T = 497.6$ and $T = 107.8$, respectively.

To elucidate the origin of the power law envelope scaling shown in Figs. 3(e) and 3(f), we analyze the temporal evolution of the amplitude $\psi_m^A(t)$ along the space-time path $m = x_0 + vt$, where v is a drift velocity. This quantity can be expressed in terms of the world-line Green's function $G_{AA}(m, x_0; t)$ [86, 101], yielding:

$$G_{AA}(m, x_0; t) = \sum_{n=\pm} \int_0^{2\pi} \frac{dk}{2\pi} g_{1,n}^{AA}(k) e^{-i[E_n(k) - kv]t}. \quad (24)$$

For convenience, momentum k is used as the integration variable instead of the Bloch phase factor $\beta = e^{ik}$. In the long-time limit, the dynamics of $G_{AA}(m, x_0; t)$ is determined by the saddle points of the function $f_n(k) = E_n(k) - kv$. Since v is real, $f_n(k)$ has the same imaginary part as $E_n(k)$, resulting in $\text{Im}f_n(k) \leq 0$ for $k \in (0, 2\pi]$. When the drift velocity v equals the group velocity at an imaginary gap-closing point k_0 , i.e., $v = v_{n,g}(k_0)$, we can expand $f_n(k)$ around k_0 with $\text{Im}f_n(k_0) = 0$. At this point, we have $(dE_n/dk)|_{k=k_0} = v_{n,g}(k_0)$, implying that k_0 is a saddle point of $f_n(k)$. Specifically, for the case where $|t_0| < |2t_1|$ and $t_0 \neq 0$, we find $(df_n/dk)|_{k_0} = 0$

and $(d^2f_n/dk^2)|_{k_0} \neq 0$. This indicates that k_0 is a second-order saddle point of $f_n(k)$. Applying the saddle-point approximation reveals that the world-line Green's function $G_{AA}(m, x_0; t)$ exhibits a $t^{-1/2}$ power-law scaling at large t . This theoretical result is confirmed by our numerical simulations, as shown in Fig. 4(a). In contrast, when $|t_0| = |2t_1|$, we have $(df_n/dk)|_{k_0} = (d^2f_n/dk^2)|_{k_0} = 0$ and $(d^3f_n/dk^3)|_{k_0} \neq 0$. Thus, the imaginary gap-closing point k_0 becomes a third-order saddle point of $f_n(k)$. Using a higher-order saddle-point approximation, we find that $G_{AA}(m, x_0; t)$ now decays as a $t^{-1/3}$ power-law scaling at large t , which agrees well with the numerical results shown in Fig. 4(b). Therefore, the power-law envelope of $G_A(x_0; t)$ observed in Figs. 3(e) and 3(f) on long time scales can be understood as follows. Considering $m = qL$, where q is a positive integer, the word-line Green's function $G_{AA}(m, x_0; t)$ is equal to the local Green's function $G_A(x_0; t)$, due to the periodic boundary conditions. Hence, $G_A(x_0; t)$ obeys the same power-law decay as $G_{AA}(m, x_0; t)$ when the drift velocity v equals $v_{n,g}(k_0)$. The corresponding total evolution time is $t = m/|v_{n,g}(k_0)| = qT$, with the period $T = L/|v_{n,g}(k_0)|$.

The preceding discussion can be extended to a more general case. If the imaginary gap-closing point k_0 is an n' -th order saddle point of $f_l(k)$, such that $(d^p f_l/dk^p)|_{k_0} = 0$ for $p = 1, 2, \dots, n' - 1$ and $(d^{n'} f_l/dk^{n'})|_{k_0} \neq 0$, the time evolution of $G_{AA}(m, x_0; t)$ can be evaluated using a higher-order saddle point approximation. Applying this method yields the asymptotic expression:

$$G_{AA}(m, x_0; t) \sim \frac{g_{1,n}^{AA}(k_0) \Gamma(1/n')}{n' \left[-f_l^{(n')}(k_0) / (n'!) \right]^{1/n'}} t^{-1/n'}. \quad (25)$$

This result implies that $G_{AA}(m, x_0; t)$ exhibits a characteristic scaling $t^{-1/n'}$. Consequently, the local Green's function $G_A(x_0; t)$ obeys the same power-law envelope scaling.

At the end of this section, we briefly examine the imaginary gap closing of the OBC spectrum. In a general non-Hermitian system, a point-gap nontrivial PBC E_{PBC} spectrum encloses the corresponding OBC spectrum E_{OBC} , resulting in the relation $\max[\text{Im}E_{OBC}] \leq \max[\text{Im}E_{PBC}]$, where equality generally cannot be attained [39]. Consequently, for dissipative systems featuring the NHSE, the OBC spectrum typically does not satisfy the imaginary gap-closing condition. To enable the OBC spectrum of the Hamiltonian (17) to satisfy $\max[\text{Im}E_{OBC}] = 0$, additional gain can be introduced to the entire system. This shifts the endpoints of the OBC spectrum onto the $\text{Re}E$ axis. In this case, the saddle-point method remains applicable to the OBC system. However, the scaling behavior of the local Green's function becomes dependent on the site x_0 : $G_A(x_0; t)$ exhibits a $t^{-1/2}$ scaling in the bulk but a $t^{-3/2}$ scaling at the edge [87].

V. SUMMARY AND DISCUSSION

In summary, this work investigates the time evolution of quantum particles in dissipative systems with imaginary gap closing. We find that the long-time dynamics are governed by both imaginary gap-closing points and saddle points. For systems with a trivial point gap, these two types of points can coincide, resulting in a single scaling behavior characterized by an asymptotic power-law decay of the local Green's function, proportional to $t^{-1/n}$, where n is the order of the saddle point. In contrast, for systems with a nontrivial point gap, the imaginary gap-closing points generally do not coincide with the saddle points, leading to two distinct dynamical regimes. In the short-time regime, the evolution is dominated by the relevant saddle points and exhibits an asymptotic exponential decay. In the long-time regime, the dynamics are controlled by the imaginary gap-closing points, which also act as saddle points of the world-line Green's function, resulting in an asymptotic power-law decay envelope scaling as $t^{-1/n'}$. These findings are supported by both theoretical analysis, via the saddle-point approximation method, and numerical simulations of concrete models. Furthermore, the framework established here can be extended to other non-Hermitian systems and may be experimentally verified on platforms such as active mechanical metamaterials, electrical circuits, optical systems, and cold atom setups.

ACKNOWLEDGMENTS

The authors thank Xinyuan Gao for helpful discussion. This work is supported by the Quantum Science and Technology-National Science and Technology Major Project (2024ZD0300600). We acknowledge financial support from the National Natural Science Foundation of China under Grant No. 92565105 and 12204395, Hong Kong RGC No. 14301425, No. 24308323, and No. C4050-23GF, Guangdong Provincial Quantum Science Strategic Initiative GDZX2404004, GDZX2505005, the Space Application System of China Manned Space Program, and CUHK Direct Grant. Jinghui Pi also acknowledges support from the Postdoctoral Fellowship Program of CPSF under Grant No. 2025M773387.

Appendix A: Saddle points of the analytical function

In this appendix, we discuss the properties of saddle points in the complex plane. For an analytic function $f(z)$ with complex variable $z = x + iy$, we consider the points where the derivative is zero, that is, $df(z)/dz = 0$. In the following, we show that such points are always saddle points. By denoting $f(z) = u(x, y) + iv(x, y)$, it follows that $u(x, y)$ and $v(x, y)$ satisfy the celebrated

Cauchy-Riemann equations:

$$\frac{\partial u}{\partial x} = \frac{\partial v}{\partial y}, \quad \frac{\partial u}{\partial y} = -\frac{\partial v}{\partial x}. \quad (\text{A1})$$

As a result, the real part u and the imaginary part v are both harmonic functions, which satisfy Laplace's equations:

$$\frac{\partial^2 u}{\partial x^2} + \frac{\partial^2 u}{\partial y^2} = 0, \quad \frac{\partial^2 v}{\partial x^2} + \frac{\partial^2 v}{\partial y^2} = 0. \quad (\text{A2})$$

These equations indicate that the second derivatives in the x and y directions are always opposite. Therefore, at a critical point z_0 where $df(z)/dz = 0$, z_0 is a saddle point for both u and v . For example, if $u(z_0)$ is a local maximum in the x direction (i.e., $\frac{\partial^2 u}{\partial x^2} < 0$), then $u(z_0)$ is also a local minimum in the y direction (i.e., $\frac{\partial^2 u}{\partial y^2} > 0$).

Furthermore, the saddle point can be related to the steepest descent/ascent lines of $v(x, y)$. The gradient of $v(x, y)$ corresponds to the vector field $(\partial v/\partial x, \partial v/\partial y)$, and the streamlines of this vector field are determined by:

$$\frac{dx}{(\partial v/\partial x)} = \frac{dy}{(\partial v/\partial y)}. \quad (\text{A3})$$

On the other hand, condition $\text{Re } f(z) = \text{Re } f(z_0)$ defines several curves along which the total derivative of $u(x, y)$ is zero. Thus, these curves satisfy the following equation:

$$\frac{dy}{dx} = -\frac{(\partial u/\partial x)}{(\partial u/\partial y)}. \quad (\text{A4})$$

According to the Cauchy-Riemann equations (A1), these curves coincide with the streamlines of the vector field $\nabla v(x, y)$. Therefore, these curves follow either the direction of the steepest ascent of $v(x, y)$ or the direction of the steepest descent. For a given saddle point z_0 , the conditions that (i) $u(x, y)$ is stationary and (ii) $\text{Im } v(x, y)$ is maximized at the point $z_0 \in J$ imply that the choice of J is unique. It comprises the two streamlines that originate from z_0 and follow the direction of steepest change in $v(x, y)$.

Appendix B: Saddle point approximation method

In this appendix, we provide a detailed discussion of the saddle-point (or steepest-descent) method. The central aim of this method is to calculate the asymptotic expression for integrals of the form $\int g(z) e^{\lambda f(z)} dz$ in the limit of a large parameter λ .

When the integration variable is a real number, such an integral can be evaluated using Laplace's method. Specifically, for a real integral $I(\lambda) = \int_a^b g(x) e^{\lambda f(x)} dx$, if $f(x)$ attains its unique maximum within the interval at a point $c \in (a, b)$, then as $\lambda \rightarrow \infty$, the integral has the

asymptotic form:

$$I(\lambda) \sim \sqrt{\frac{2\pi}{-\lambda f''(c)}} g(c) e^{\lambda f(c)}. \quad (\text{B1})$$

This expression holds provided that $f''(c) \neq 0$ and $g(c) \neq 0$. As the integrand is sharply peaked around c for large λ , one can approximate $f(x)$ by its Taylor expansion around c up to the second order and perform a Gaussian integral to obtain the dominant part of the integral. If $f(x)$ has more than one local maximum, correction terms for the asymptotic expression arise at large but finite λ . One can perform a similar Gaussian-integral approximation around each individual local maximum c_i , leading to:

$$I(\lambda) \sim \sum_i \sqrt{\frac{2\pi}{-\lambda f''(c_i)}} g(c_i) e^{\lambda f(c_i)}. \quad (\text{B2})$$

When the integration is a contour integral, such as $\oint_{\mathcal{C}} g(z) e^{\lambda f(z)} dz$ in the complex z -plane, we parametrize the contour \mathcal{C} with $z = \gamma(x)$. In this case, the dominant part of the integral is determined by the maxima of $\text{Re } f(x)$, and we can still employ Laplace's approximation. As $\text{Re } f(x)$ reaches its maximum value

at $x = c$, in the neighborhood of c , we have:

$$f(x) \approx f(c) + i\lambda(x - c) \text{Im } f'(c) + \frac{\lambda(x - c)^2}{2} f''(c). \quad (\text{B3})$$

Therefore, the additional factor $e^{i\lambda(x-c) \text{Im } f'(c)}$ oscillates strongly for large λ , making the Gaussian integral indeterminate. However, by Cauchy's theorem, we can deform the contour \mathcal{C} into a new contour \mathcal{C}' without altering the integral's value. To facilitate the calculation, the new contour \mathcal{C}' is chosen such that $\text{Im } f(z)$ is constant along the path \mathcal{C}' . In addition, there is a point $z_s \in \mathcal{C}'$ where $\text{Re } f(z)$ attains its maximal value on \mathcal{C}' . Under these two conditions, we can safely use Laplace's approximation and obtain the asymptotic expression:

$$I(\lambda) \sim \sqrt{\frac{2\pi}{-\lambda f''(z_s)}} g(z_s) e^{\lambda f(z_s)}. \quad (\text{B4})$$

This is valid provided that $f''(z_s) \neq 0$ and $g(z_s) \neq 0$. By denoting $z_s = \gamma(c)$, it is straightforward to show that $\frac{d}{dx} f(\gamma(c)) = \gamma'(c) f'(z_s) = 0$. Since $\gamma'(x)$ should be non-vanishing for non-singular parametrization, it follows that $f'(z_s) = 0$. As a result, z_s is a saddle point of $f(z)$. The integral (B4) is asymptotically dominated by the neighborhood of z_s , similar to the real case. This suggests that other parts of the contour of integration are less relevant, and the condition on the contour \mathcal{C}' can be relaxed. Specifically, the requirement that $\text{Im } f$ remains constant along the entire contour \mathcal{C}' can be relaxed to it being stationary near z_s .

[1] C. M. Bender, Making sense of non-Hermitian Hamiltonians, *Rep. Prog. Phys.* **70**, 947 (2007).

[2] H. Cao and J. Wiersig, Dielectric microcavities: Model systems for wave chaos and non-Hermitian physics, *Rev. Mod. Phys.* **87**, 61 (2015).

[3] V. V. Konotop, J. Yang, and D. A. Zezyulin, Nonlinear waves in \mathcal{PT} -symmetric systems, *Rev. Mod. Phys.* **88**, 035002 (2016).

[4] R. El-Ganainy, K. G. Makris, M. Khajavikhan, Z. H. Musslimani, S. Rotter, and D. N. Christodoulides, Non-Hermitian physics and \mathcal{PT} symmetry, *Nat. Phys.* **14**, 11 (2018).

[5] Y. Ashida, Z. Gong, and M. Ueda, Non-Hermitian physics, *Adv. Phys.* **69**, 249 (2020).

[6] E. J. Bergholtz, J. C. Budich, and F. K. Kunst, Exceptional topology of non-Hermitian systems, *Rev. Mod. Phys.* **93**, 015005 (2021).

[7] N. Okuma and M. Sato, Non-Hermitian topological phenomena: A review, *Annu. Rev. Condens. Matter Phys.* **14**, 83 (2023).

[8] C. E. Rüter, K. G. Makris, R. El-Ganainy, D. N. Christodoulides, M. Segev, and D. Kip, Observation of parity-time symmetry in optics, *Nat. Phys.* **6**, 192 (2010).

[9] Y. D. Chong, L. Ge, and A. D. Stone, \mathcal{PT} -symmetry breaking and laser-absorber modes in optical scattering systems, *Phys. Rev. Lett.* **106**, 093902 (2011).

[10] A. Regensburger, C. Bersch, M.-A. Miri, G. Onishchukov, D. N. Christodoulides, and U. Peschel, Parity-time synthetic photonic lattices, *Nature* **488**, 167 (2012).

[11] B. Peng, S. K. Özdemir, F. Lei, F. Monifi, M. Gianfreda, G. L. Long, S. Fan, F. Nori, C. M. Bender, and L. Yang, Parity-time-symmetric whispering-gallery microcavities, *Nat. Phys.* **10**, 394 (2014).

[12] L. Feng, R. El-Ganainy, and L. Ge, Non-Hermitian photonics based on parity-time symmetry, *Nat. Photon.* **11**, 752 (2017).

[13] S. Longhi, Parity-time symmetry meets photonics: A new twist in non-Hermitian optics, *Europhys. Lett.* **120**, 64001 (2018).

[14] M. Ezawa, Non-Hermitian higher-order topological states in nonreciprocal and reciprocal systems with their electric-circuit realization, *Phys. Rev. B* **99**, 201411 (2019).

[15] T. Hofmann, T. Helbig, F. Schindler, N. Salgo, M. Brzezińska, M. Greiter, T. Kiessling, D. Wolf, A. Vollhardt, A. Kabaši, C. H. Lee, A. Bilušić, R. Thomale, and T. Neupert, Reciprocal skin effect and its realization in a topoelectrical circuit, *Phys. Rev. Res.*

2, 023265 (2020).

[16] T. Helbig, T. Hofmann, S. Imhof, M. Abdelghany, T. Kiessling, L. Molenkamp, C. Lee, A. Szameit, M. Greiter, and R. Thomale, Generalized bulk-boundary correspondence in non-Hermitian topoelectrical circuits, *Nat. Phys.* **16**, 747 (2020).

[17] X.-X. Zhang and M. Franz, Non-Hermitian exceptional Landau quantization in electric circuits, *Phys. Rev. Lett.* **124**, 046401 (2020).

[18] X. Zhang, Y. Tian, J.-H. Jiang, M.-H. Lu, and Y.-F. Chen, Observation of higher-order non-Hermitian skin effect, *Nat. Commun.* **12**, 5377 (2021).

[19] D. Zou, T. Chen, W. He, J. Bao, C. H. Lee, H. Sun, and X. Zhang, Observation of hybrid higher-order skin-topological effect in non-Hermitian topoelectrical circuits, *Nat. Commun.* **12**, 7201 (2021).

[20] A. Wang, Z. Meng, and C. Q. Chen, Non-Hermitian topology in static mechanical metamaterials, *Sci. Adv.* **9**, eadft299 (2023).

[21] W. Wang, M. Hu, X. Wang, G. Ma, and K. Ding, Experimental Realization of Geometry-Dependent Skin Effect in a Reciprocal Two-Dimensional Lattice, *Phys. Rev. Lett.* **131**, 207201 (2023).

[22] Y.-K. Liu, P.-C. Cao, M. Qi, Q.-K.-L. Huang, F. Gao, Y.-G. Peng, Y. Li, and X.-F. Zhu, Observation of non-Hermitian skin effect in thermal diffusion, *Sci. Bull.* **69**, 1228 (2024).

[23] X. Zhang, B. Zhang, W. Zhao, and C. H. Lee, Observation of non-local impedance response in a passive electrical circuit, *SciPost Phys.* **16**, 002 (2024).

[24] S. Zhang and Z. H. Hang, Photonic realization of non-Hermitian skin effect using topological ring cavities, *Rev. Phys.* **13**, 100102 (2025).

[25] T. Yoshida, R. Peters, and N. Kawakami, Non-Hermitian perspective of the band structure in heavy-fermion systems, *Phys. Rev. B* **98**, 035141 (2018).

[26] H. Shen and L. Fu, Quantum Oscillation from In-Gap States and a Non-Hermitian Landau Level Problem, *Phys. Rev. Lett.* **121**, 026403 (2018).

[27] K. Yamamoto, M. Nakagawa, K. Adachi, K. Takasan, M. Ueda, and N. Kawakami, Theory of Non-Hermitian Fermionic Superfluidity with a Complex-Valued Interaction, *Phys. Rev. Lett.* **123**, 123601 (2019).

[28] Y. Nagai, Y. Qi, H. Isobe, V. Kozii, and L. Fu, DMFT Reveals the Non-Hermitian Topology and Fermi Arcs in Heavy-Fermion Systems, *Phys. Rev. Lett.* **125**, 227204 (2020).

[29] S. Kaneshiro, T. Yoshida, and R. Peters, \mathbb{Z}_2 non-Hermitian skin effect in equilibrium heavy-fermion systems, *Phys. Rev. B* **107**, 195149 (2023).

[30] R. Zheng, J. Lin, J. Liang, K. Ding, J. Lu, W. Deng, M. Ke, X. Huang, and Z. Liu, Experimental probe of point gap topology from non-Hermitian Fermi-arcs, *Commun. Phys.* **7**, 298 (2024).

[31] V. Kozii and L. Fu, Non-Hermitian topological theory of finite-lifetime quasiparticles: Prediction of bulk Fermi arc due to exceptional point, *Phys. Rev. B* **109**, 235139 (2024).

[32] S. Yao and Z. Wang, Edge States and Topological Invariants of Non-Hermitian Systems, *Phys. Rev. Lett.* **121**, 086803 (2018).

[33] S. Yao, F. Song, and Z. Wang, Non-Hermitian Chern Bands, *Phys. Rev. Lett.* **121**, 136802 (2018).

[34] V. M. Martinez Alvarez, J. E. Barrios Vargas, and L. E. F. Foa Torres, Non-Hermitian robust edge states in one dimension: Anomalous localization and eigenspace condensation at exceptional points, *Phys. Rev. B* **97**, 121401(R) (2018).

[35] C. H. Lee and R. Thomale, Anatomy of skin modes and topology in non-Hermitian systems, *Phys. Rev. B* **99**, 201103 (2019).

[36] C. H. Lee, L. Li, and J. Gong, Hybrid Higher-Order Skin-Topological Modes in Nonreciprocal Systems, *Phys. Rev. Lett.* **123**, 016805 (2019).

[37] K. Kawabata, M. Sato, and K. Shiozaki, Higher-order non-Hermitian skin effect, *Phys. Rev. B* **102**, 205118 (2020).

[38] K. Kawabata, K. Shiozaki, M. Ueda, and M. Sato, Symmetry and Topology in Non-Hermitian Physics, *Phys. Rev. X* **9**, 041015 (2019).

[39] N. Okuma, K. Kawabata, K. Shiozaki, and M. Sato, Topological Origin of Non-Hermitian Skin Effects, *Phys. Rev. Lett.* **124**, 086801 (2020).

[40] D. Nakamura, T. Bessho, and M. Sato, Bulk-Boundary Correspondence in Point-Gap Topological Phases, *Phys. Rev. Lett.* **132**, 136401 (2024).

[41] D. S. Borgnia, A. J. Kruchkov, and R.-J. Slager, Non-Hermitian Boundary Modes and Topology, *Phys. Rev. Lett.* **124**, 056802 (2020).

[42] L. Xiao, T. Deng, K. Wang, G. Zhu, Z. Wang, W. Yi, and P. Xue, Non-Hermitian bulk-boundary correspondence in quantum dynamics, *Nat. Phys.* **16**, 761 (2020).

[43] A. Ghatak, M. Brandenburger, J. van Wezel, and C. Coulais, Observation of non-Hermitian topology and its bulk-edge correspondence in an active mechanical metamaterial, *PNAS* **117**, 29561 (2020).

[44] F. Song, S. Yao, and Z. Wang, Non-Hermitian Topological Invariants in Real Space, *Phys. Rev. Lett.* **123**, 246801 (2019).

[45] K. Yokomizo and S. Murakami, Non-Bloch Band Theory of non-Hermitian Systems, *Phys. Rev. Lett.* **123**, 066404 (2019).

[46] K. Zhang, Z. Yang, and C. Fang, Correspondence between Winding Numbers and Skin Modes in non-Hermitian Systems, *Phys. Rev. Lett.* **125**, 126402 (2020).

[47] C.-X. Guo, C.-H. Liu, X.-M. Zhao, Y. Liu, and S. Chen, Exact Solution of Non-Hermitian Systems with Generalized Boundary Conditions: Size-Dependent Boundary Effect and Fragility of the Skin Effect, *Phys. Rev. Lett.* **127**, 116801 (2021).

[48] L. Li, S. Mu, C. H. Lee, and J. Gong, Quantized classical response from spectral winding topology, *Nat. Commun.* **12**, 5294 (2021).

[49] K. Zhang, Z. Yang, and C. Fang, Universal non-Hermitian skin effect in two and higher dimensions, *Nat. Commun.* **13**, 2496 (2022).

[50] H.-Y. Wang, F. Song, and Z. Wang, Amoeba Formulation of Non-Bloch Band Theory in Arbitrary Dimensions, *Phys. Rev. X* **14**, 021011 (2024).

[51] H. Lin, J. Pi, Y. Qi, W. Qin, F. Nori, and G.-L. Long, Imaginary-Stark skin effect, *Phys. Rev. Res.* **7**, 033150 (2025).

[52] E. M. Kessler, G. Giedke, A. Imamoglu, S. F. Yelin, M. D. Lukin, and J. I. Cirac, Dissipative phase transition in a central spin system, *Phys. Rev. A* **86**, 012116 (2012).

[53] M. Höning, M. Moos, and M. Fleischhauer, Critical exponents of steady-state phase transitions in fermionic lattice models, *Phys. Rev. A* **86**, 013606 (2012).

[54] B. Horstmann, J. I. Cirac, and G. Giedke, Noise-driven dynamics and phase transitions in fermionic systems, *Phys. Rev. A* **87**, 012108 (2013).

[55] F. Minganti, A. Biella, N. Bartolo, and C. Ciuti, Spectral theory of Liouvillians for dissipative phase transitions, *Phys. Rev. A* **98**, 042118 (2018).

[56] Z. Cai and T. Barthel, Algebraic versus Exponential Decoherence in Dissipative Many-Particle Systems, *Phys. Rev. Lett.* **111**, 150403 (2013).

[57] L. Bonnes, D. Charrier, and A. M. Läuchli, Dynamical and steady-state properties of a Bose-Hubbard chain with bond dissipation: A study based on matrix product operators, *Phys. Rev. A* **90**, 033612 (2014).

[58] M. Žnidarič, Relaxation times of dissipative many-body quantum systems, *Phys. Rev. E* **92**, 042143 (2015).

[59] F. Song, S. Yao, and Z. Wang, Non-Hermitian Skin Effect and Chiral Damping in Open Quantum Systems, *Phys. Rev. Lett.* **123**, 170401 (2019).

[60] T. Haga, M. Nakagawa, R. Hamazaki, and M. Ueda, Liouvillian Skin Effect: Slowing Down of Relaxation Processes without Gap Closing, *Phys. Rev. Lett.* **127**, 070402 (2021).

[61] C.-H. Liu, K. Zhang, Z. Yang, and S. Chen, Helical damping and dynamical critical skin effect in open quantum systems, *Phys. Rev. Res.* **2**, 043167 (2020).

[62] T. Mori and T. Shirai, Resolving a Discrepancy between Liouvillian Gap and Relaxation Time in Boundary-Dissipated Quantum Many-Body Systems, *Phys. Rev. Lett.* **125**, 230604 (2020).

[63] F. Yang, Q.-D. Jiang, and E. J. Bergholtz, Liouvillian skin effect in an exactly solvable model, *Phys. Rev. Res.* **4**, 023160 (2022).

[64] S. Ma, H. Lin, and J. Pi, Imaginary gap-closed points and dynamics in a class of dissipative systems, *Phys. Rev. B* **109**, 214311 (2024).

[65] A. McDonald, T. Pereg-Barnea, and A. A. Clerk, Phase-Dependent Chiral Transport and Effective Non-Hermitian Dynamics in a Bosonic Kitaev-Majorana Chain, *Phys. Rev. X* **8**, 041031 (2018).

[66] C. C. Wanjura, M. Brunelli, and A. Nunnenkamp, Topological framework for directional amplification in driven-dissipative cavity arrays, *Nat. Commun.* **11**, 3149 (2020).

[67] W.-T. Xue, M.-R. Li, Y.-M. Hu, F. Song, and Z. Wang, Simple formulas of directional amplification from non-Bloch band theory, *Phys. Rev. B* **103**, L241408 (2021).

[68] H.-K. Lau and A. A. Clerk, Fundamental limits and non-reciprocal approaches in non-Hermitian quantum sensing, *Nat. Commun.* **9**, 4320 (2018).

[69] A. McDonald and A. A. Clerk, Exponentially-enhanced quantum sensing with non-Hermitian lattice dynamics, *Nat. Commun.* **11**, 5382 (2020).

[70] J. C. Budich and E. J. Bergholtz, Non-Hermitian Topological Sensors, *Phys. Rev. Lett.* **125**, 180403 (2020).

[71] F. Koch and J. C. Budich, Quantum non-Hermitian topological sensors, *Phys. Rev. Res.* **4**, 013113 (2022).

[72] X. Chen, Y. Li, M. P. A. Fisher, and A. Lucas, Emergent conformal symmetry in nonunitary random dynamics of free fermions, *Phys. Rev. Res.* **2**, 033017 (2020).

[73] S. Gopalakrishnan and M. J. Gullans, Entanglement and Purification Transitions in Non-Hermitian Quantum Mechanics, *Phys. Rev. Lett.* **126**, 170503 (2021).

[74] S.-K. Jian, Z.-C. Yang, Z. Bi, and X. Chen, Yang-Lee edge singularity triggered entanglement transition, *Phys. Rev. B* **104**, L161107 (2021).

[75] X. Turkeshi and M. Schiró, Entanglement and correlation spreading in non-Hermitian spin chains, *Phys. Rev. B* **107**, L020403 (2023).

[76] K. Kawabata, T. Numasawa, and S. Ryu, Entanglement Phase Transition Induced by the Non-Hermitian Skin Effect, *Phys. Rev. X* **13**, 021007 (2023).

[77] S. Longhi, Self-Healing of Non-Hermitian Topological Skin Modes, *Phys. Rev. Lett.* **128**, 157601 (2022).

[78] K. Zhang, C. Fang, and Z. Yang, Dynamical Degeneracy Splitting and Directional Invisibility in Non-Hermitian Systems, *Phys. Rev. Lett.* **131**, 036402 (2023).

[79] W.-T. Xue, Y.-M. Hu, F. Song, and Z. Wang, Non-Hermitian Edge Burst, *Phys. Rev. Lett.* **128**, 120401 (2022).

[80] L. Xiao, W.-T. Xue, F. Song, Y.-M. Hu, W. Yi, Z. Wang, and P. Xue, Observation of Non-Hermitian Edge Burst in Quantum Dynamics, *Phys. Rev. Lett.* **133**, 070801 (2024).

[81] P. Wen, J. Pi, and G.-L. Long, Investigation of a non-Hermitian edge burst with time-dependent perturbation theory, *Phys. Rev. A* **109**, 022236 (2024).

[82] L. Mao, T. Deng, and P. Zhang, Boundary condition independence of non-Hermitian Hamiltonian dynamics, *Phys. Rev. B* **104**, 125435 (2021).

[83] X. Yang, C. Tan, Y. Yan, and R. Zhang, Non-Hermitian Thouless pumping: Interplay between topological charge pumping and directional tunneling, *Phys. Rev. A* **111**, 053308 (2025).

[84] N. Bleistein and R. A. Handelsman, *Asymptotic Expansions of Integrals* (Dover Publications, Inc., New York, 1986).

[85] Y. Yi and Z. Yang, Non-Hermitian Skin Modes Induced by On-Site Dissipations and Chiral Tunneling Effect, *Phys. Rev. Lett.* **125**, 186802 (2020).

[86] W.-T. Xue, F. Song, Y.-M. Hu, and Z. Wang, Non-Bloch edge dynamics of non-Hermitian lattices, *arXiv:2503.13671*.

[87] T.-H. Yang and C. Fang, Real-Time Edge Dynamics of Non-Hermitian Lattices, *Phys. Rev. Lett.* **135**, 186401 (2025).

[88] Z. Yang, K. Zhang, C. Fang, and J. Hu, Non-Hermitian Bulk-Boundary Correspondence and Auxiliary Generalized Brillouin Zone Theory, *Phys. Rev. Lett.* **125**, 226402 (2020).

[89] Zhou, Kunling and Zhao, Jun and Zeng, Bowen and Hu, Yong, Abnormal frequency response determined by saddle points in non-Hermitian crystals, *Phys. Rev. B* **110**, L140302 (2024).

[90] J. Pi, C. Wang, Y.-C. Liu, and Y. Yan, Geometric origin of self-intersection points in non-Hermitian energy spectra, *Phys. Rev. B* **111**, 165407 (2025).

[91] J. W. Milnor, *Morse theory*, 51 (Princeton university press, 1963).

[92] Y. Matsumoto, *An introduction to Morse theory*, Vol. 208 (American Mathematical Soc., 2002).

[93] M. V. Berry and C. J. Howls, Hyperasymptotics for integrals with saddles, *Proc. R. Soc. A* **434**, 657 (1991).

[94] C. Howls, Hyperasymptotics for multidimensional integrals, exact remainder terms and the global connection

problem, *Proc. R. Soc. A* **453**, 2271 (1997).

[95] F. Pham, Vanishing homologies and the n variables saddlepoint method, in *Proc. Symp. Pure Math.*, Vol. 40 (1983) pp. 310–333.

[96] E. Witten, Analytic continuation of chern-simons theory, *AMS/IP Stud. Adv. Math* **50**, 347 (2011).

[97] A. Mukherjee and M. Cristoforetti, Lefschetz thimble Monte Carlo for many-body theories: A Hubbard model study, *Phys. Rev. B* **90**, 035134 (2014).

[98] T. Kanazawa and Y. Tanizaki, Structure of Lefschetz thimbles in simple fermionic systems, *J. High Energy Phys.* **2015** (3), 1.

[99] E. H. Lieb and D. W. Robinson, The finite group velocity of quantum spin systems, *Commun. Math. Phys.* **28**, 251 (1972).

[100] Z. Gong, Y. Ashida, K. Kawabata, K. Takasan, S. Higashikawa, and M. Ueda, Topological Phases of Non-Hermitian Systems, *Phys. Rev. X* **8**, 031079 (2018).

[101] S. Longhi, Probing non-Hermitian skin effect and non-Bloch phase transitions, *Phys. Rev. Res.* **1**, 023013 (2019).